





Cite this: *Nanoscale*, 2018, **10**, 16692

Atomically sharp interlayer stacking shifts at anti-phase grain boundaries in overlapping MoS₂ secondary layers†

Si Zhou,^a Shanshan Wang,^{a,b} Zhe Shi,^c Hidetaka Sawada,^d Angus I. Kirkland,^{a,e} Ju Li ^{c,f} and Jamie H. Warner ^{*a}

When secondary domains nucleate and grow on the surface of monolayer MoS₂, they can extend across grain boundaries in the underlying monolayer MoS₂ and form overlapping sections. We present an atomic level study of overlapping antiphase grain boundaries (GBs) in MoS₂ monolayer-bilayers using aberration-corrected annular dark field scanning transmission electron microscopy. In particular we focus on the antiphase GB within a monolayer and track its propagation through an overlapping bilayer domain. We show that this leads to an atomically sharp interface between 2H and 3R interlayer stacking in the bilayer region. We have studied the micro-nanoscale “meandering” of the antiphase GB in MoS₂, which shows a directional dependence on the density of 4 and 8 member ring defects, as well as sharp turning angles 90°–100° that are mediated by a special 8-member ring defect. Density functional theory has been used to explore the overlapping interlayer stacking around the antiphase GBs, confirming our experimental findings. These results show that overlapping secondary bilayer MoS₂ domains cause atomic structure modification to underlying anti-phase GB sites to accommodate the van der Waals interactions.

Received 2nd June 2018,
Accepted 19th August 2018
DOI: 10.1039/c8nr04486d

rsc.li/nanoscale

Introduction

MoS₂ is a semiconducting transition metal dichalcogenide (TMD) with a direct band gap in monolayer form, and indirect in the bulk.^{1–4} It offers a band gap in the red visible spectrum and semiconducting properties that expand the applications for 2D materials beyond what graphene can achieve.^{5–7} Moreover, large-area monolayer MoS₂ can be synthesized using CVD,^{8–11} making it a promising candidate for building atomically thin, layered electrical, optical, and photovoltaic devices.^{12–16} However, in the production of large-area 2D materials, grain boundaries (GBs) are inevitably produced between randomly oriented crystal domains within a polycrystalline film.^{17–19}

Conventional GBs in 3D polycrystalline and nanocrystalline solids influence their mechanical, physical and chemical properties.^{20,21} The general effects of GBs on the properties of 2D materials can be assigned to GB dislocation cores, the orientation mismatch between grains and the in-plane and out-of-plane strains introduced.²² GBs in graphene are usually formed by dislocation cores consisting of pentagon–heptagon ring pairs.^{23–25} The presence of GBs can also lead to detrimental effects on some properties of graphene, including reduced electron mobility,^{26–29} thermal conductivity,³⁰ and reduced ultimate mechanical strength.³¹ Conversely, GBs in graphene can also be beneficially exploited *via* controlled GB engineering.³²

Recently, GBs have been shown to play an important role in reducing the charge carrier mobility in monolayer MoS₂.³³ These extended defects can act as undesired sinks for carriers, increasing their scattering and degrading electrical performance.^{34,35} Individual GBs can also strongly affect the photoluminescence of MoS₂ monolayers and alter their in-plane electrical conductivity.³⁶ All of these effects strongly depend on the GB tilt angles and the local doping and strain introduced by dislocation cores.³⁶ Therefore, atomic structure analysis of these GBs can facilitate tailoring the properties of MoS₂ *via* controlled defect engineering. Dislocation cores in monolayer MoS₂ vary in configuration due to the Mo–S bonding characteristics. Structures including 5–7, 4–4, 4–6, 6–8 and 4–8 rings are both theoretically predicted and have been experimentally observed,^{36–41} and are dependent on the local Mo/S source

^aDepartment of Materials, University of Oxford, 16 Parks Road, Oxford, OX1 3PH, UK. E-mail: Jamie.warner@materials.ox.ac.uk

^bScience and Technology on Advanced Ceramic Fibers & Composites Laboratory, National University of Defense Technology, Changsha 410073, Hunan Province, China

^cDepartment of Materials Science and Engineering, MIT, 77 Massachusetts Ave, Cambridge, MA 02139, USA

^dJEOL Ltd., 3-1-2 Musashino, Akishima, Tokyo 196-8558, Japan

^eElectron Physical Sciences Imaging Center, Diamond Light Source Ltd, Didcot, UK

^fDepartment of Nuclear Science and Engineering, MIT, 77 Massachusetts Ave, Cambridge, MA 02139, USA

† Electronic supplementary information (ESI) available. See DOI: 10.1039/c8nr04486d

concentration as well as the tilt angle.³⁷ Furthermore, the misorientation angle of the tilt GB ranges from 0° to 60° due to the 3-fold symmetry of MoS₂ lattice.^{36–41}

The 60° GBs (also denoted as antiphase boundaries), are of particular interest as they form one-dimensional metallic wires in a semiconducting MoS₂ matrix,^{36–39,41,42} and act as conductive channels that have a profound influence on both transport properties and exciton behavior of the monolayers.^{37,38,43} Experimental studies have shown that a single 60° GB can enhance the in-plane electrical conductivity and substantially quench the local photoluminescence.⁴⁴ Structural studies at atomic resolution have revealed that these GBs introduce mirror symmetry between two grains, which are connected predominantly through lines of 8- and 4-membered rings.³⁷ Inversion domains surrounded by these 60° GBs are formed by annealing TMD monolayers at high temperature.³⁹ However, the micro-nanoscale distribution of the defects in antiphase GBs and their correlation to the propagation direction of the GB has yet to be studied in sufficient detail to gain an overall picture of their behavior. Furthermore, the nanoscale-microscale density and distribution of 4- and 8-rings associated with

specific directions in the antiphase GB with atomic level detail has not been fully clarified. A few studies have described the growth mechanisms of grain boundaries in MoS₂ and graphene.^{39,44–46} Studies of monolayer h-BN have shown that in polycrystalline regions two merging domains can have overlapping interface rather than atomically bonded.⁴⁷ Recent work has used ADF-STEM to study the strain maps around mirror twin grain boundaries in MoSe₂ bilayers with small grain boundaries and inversion domains, revealing strain relaxation within the local GB area.⁴⁸ However, the understanding of the behavior of GBs in monolayer-bilayer stacks on a larger size scale with dimensions extending to micron distances has yet to be explored in detail.

In this study, MoS₂ samples were grown on Si substrates with a 300 nm oxide layer using methods previously described.⁴⁹ The samples of MoS₂ produced were predominantly monolayer, with occasional small bilayer domains on top of the larger monolayer film. We used annular dark field scanning transmission electron microscopy (ADF-STEM) to probe the atomic structure of antiphase boundaries in both MoS₂ monolayers and bilayers and have studied the 4-ring and

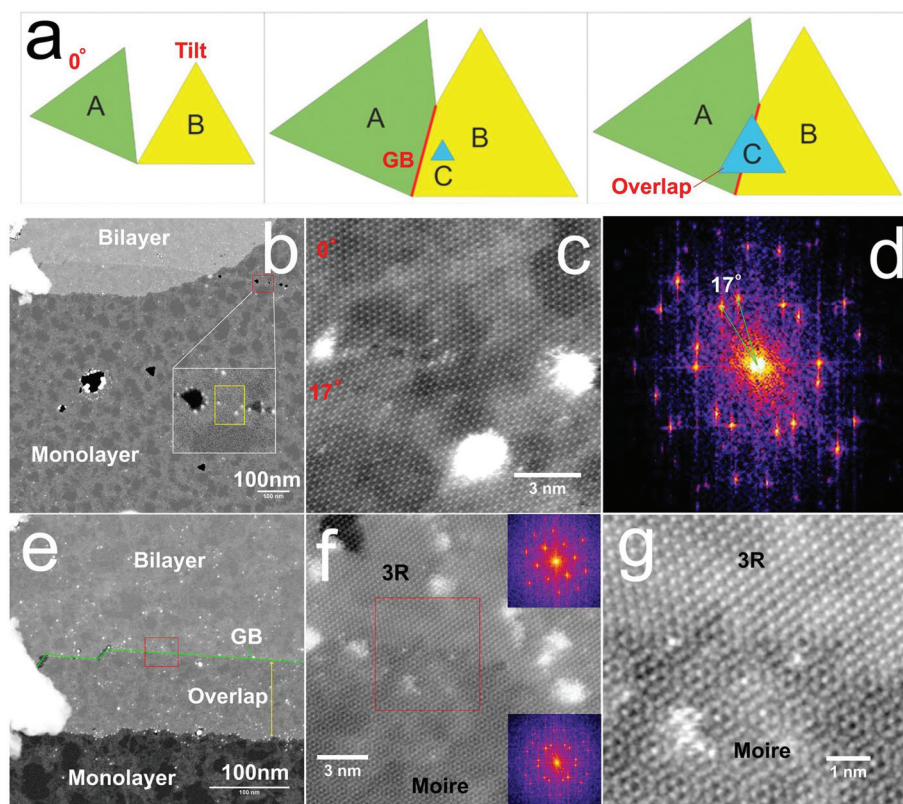


Fig. 1 (a) Schematic illustrations showing how a secondary MoS₂ layer C grows across the GB between two rotated grains A and B, forming the overlapping bilayer GB region. (b) ADF-STEM image of a tilted GB in a monolayer MoS₂ region with an overlapping bilayer section. White box inset shows the magnified view from the red box area. (c) ADF-STEM image from the yellow boxed region in (b) showing the tilted GB (17°) in the monolayer MoS₂. The three Pt nanoparticles are seen as reference points. (d) FFT power spectrum from (c) showing the two sets of spots, giving tilt angle of $\sim 17^\circ$. (e) ADF-STEM image showing the overlapping GB area from (b), with the GB indicated by the green line. (f) ADF-STEM image from the red box area in (e) showing the overlapping bilayer GB has 3R stacking on its nucleation side (top) and Moire pattern on the overlapping side (bottom). Insets show FFT power spectra from each side of the GB in the image with 17° mismatch within the two layers comprising the Moire pattern, correlating to the tilt angle. (g) Higher magnification ADF-STEM image from the red box area in (f).

8-ring defects and their relationship with the meandering GB. We have also studied how an antiphase GB propagates from a monolayer to an overlapping bilayer domain leading to modification of the 2H and 3R bilayer stacking configurations and possible growth processes for differently orientated antiphase boundaries in MoS₂ monolayers are discussed. Density functional theory (DFT) calculations have been used to provide accurate model structures for multislice image simulations for comparison with the experimental ADF-STEM images in order to understand the impact of van der Waals forces.

Results and discussion

Fig. 1a shows a schematic illustration of how two rotated monolayer MoS₂ grains (A and B) can meet to form a tilt grain boundary, as highlighted red in the second panel. A secondary MoS₂ layer (C) nucleates on top of grain B and then continues

growing to finally overlap across the top of grain A. This should lead to a GB section where one side has well defined stacking of 2H or 3R, and the other side has a Moire pattern with the orientation mismatch corresponding to the GB tilt angle. The low magnification ADF-STEM image in Fig. 1b shows a region where a secondary MoS₂ domain has grown across a tilt GB in the underlying monolayer. Fig. 1c shows the ADF-STEM image of the tilt GB in the monolayer MoS₂, taken from the red boxed area in Fig. 1(a), revealing a 17° tilt angle, Fig. 1(d). The bright nanoparticles in Fig. 1b are Pt and were intentionally deposited to help locate the GB regions easily in ADF-STEM. The ADF-STEM image in Fig. 1e shows the overlapping bilayer MoS₂ region, with the green line indicating the GB position. Fig. 1f and g shows the atomically resolved ADF-STEM images of the GB in the overlapping region, with 3R stacking at the top and Moire pattern below. This establishes that bilayer domains can grow across GBs that already exist in monolayer MoS₂. We now focus the rest of our study to

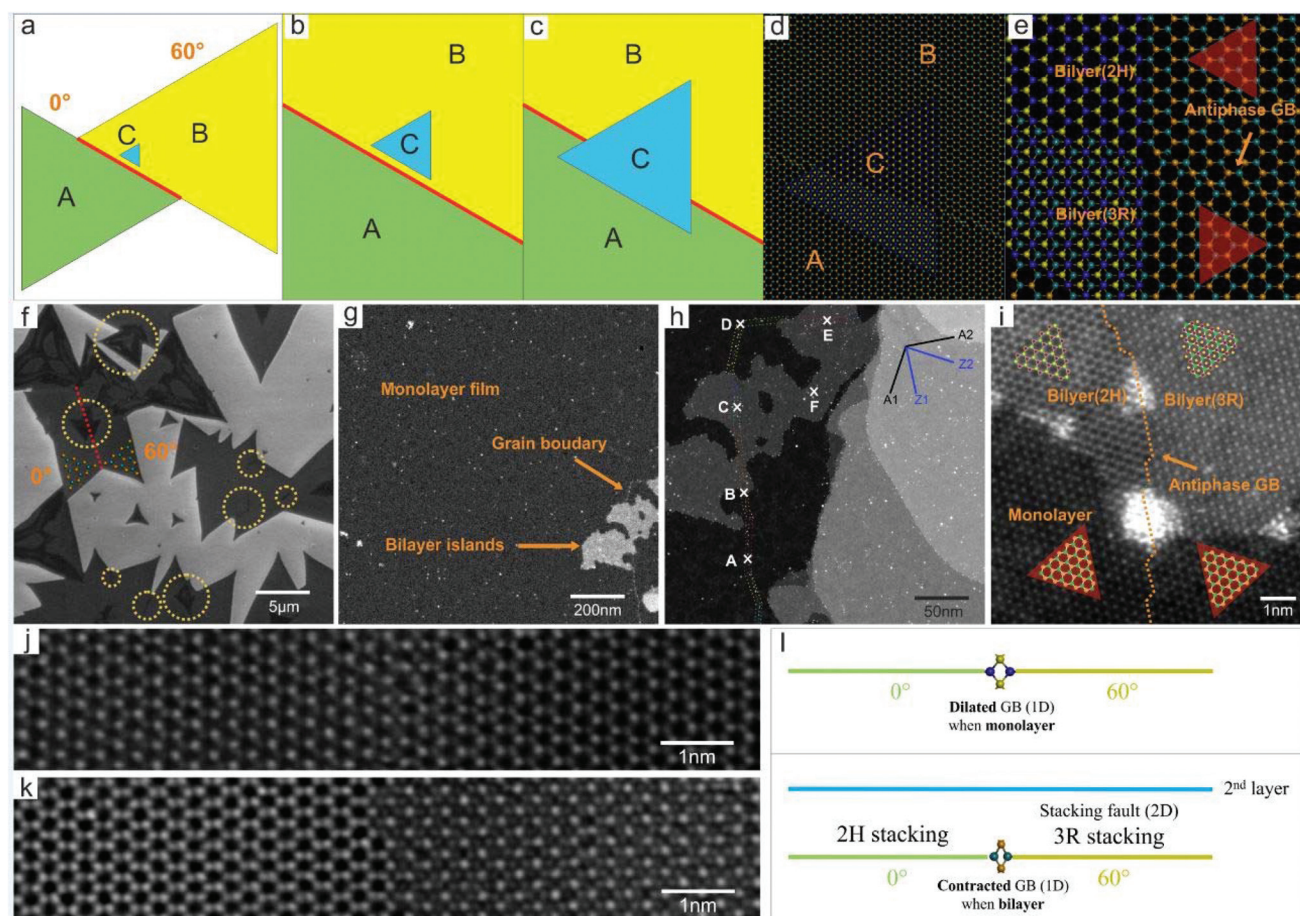


Fig. 2 (a–c) Schematics showing a secondary MoS₂ layer C growing across the GB between two 60° rotated grains A and B. (d) Atomic model based on the schematic in c. (e) Magnified image of the model showing the antiphase GB in both monolayer and bilayer regions. (f) SEM image of several secondary layers grown on top of GBs, one of which is formed between two 60° rotated grains as indicated. (g) Low magnification ADF-STEM image of continuous monolayer MoS₂ with scattered bilayer islands suspended on holey SiN TEM grid. (h) Intermediate magnification ADF-STEM image showing the propagation of a GB through monolayer and bilayer regions. Zones along the pathway of the GB are marked as A–F. A1, A2, Z1 and Z2 represent armchair and zigzag directions. (i) ADF-STEM image of the GB in both monolayer and bilayer regions. Overlaid lattice diagrams show a 60° rotation for the monolayer grains and different stacking sequences in the bilayers. (j and k) Magnified images of zone A and C, respectively. (l) Schematics showing the contraction difference between the 4-member rings in monolayer and bilayer systems.

anti-phase GBs, examining overlapping bilayer regions at anti-phase GBs, as well as the nanoscale structure of anti-phase GBs in monolayers.

The schematic in Fig. 2a, shows a secondary layer (C) growing on top of grain (B), which meets a 60° rotated grain (A) forming a grain boundary highlighted in red. Layer (C) approaches the GB during growth (Fig. 2b) and finally reaches and grows across the GB (Fig. 2c). Fig. 2d shows the atomic model of the secondary layer on top of both grain A and B corresponding to Fig. 2c which demonstrates that the GB is an antiphase GB, which introduces a 60° lattice rotation in the monolayer region (Fig. 2e). The bilayer region exhibits a 2H–3R stacking sequence with the antiphase boundary at the interface between these. Hence, a stacking sequence change is predicted when the secondary layer grows across the antiphase boundary. The SEM image in Fig. 2f shows several secondary layers grown on top of the GB (indicated by yellow dashed

circles). The secondary layers are seen by their increased contrast in the SEM image and are also found in regions where grain boundaries are expected to form at the mirror plane between two merging single crystal domains.⁵⁰ A low magnification ADF-STEM image over a large field of view of a region is shown in Fig. 2g and h, showing an antiphase GB in MoS₂ that exists within the larger monolayer that also propagates through regions containing bilayers (zone C and E). The mono-bilayer interface at zone B is magnified in Fig. 2i. Pt nanoparticles were formed at the GBs during the TEM sample preparation stage to help find the GB location at lower magnification, but do not impact the results of the interlayer stacking structure presented in this work.⁵¹ In the bilayer region, both 2H and 3R stacking sequences are observed with the antiphase GB at the interface. Magnified images at zone A and C are displayed in Fig. 2j and k, respectively. Fig. 2j shows octagonal and quadrangular configurations as the structural build-

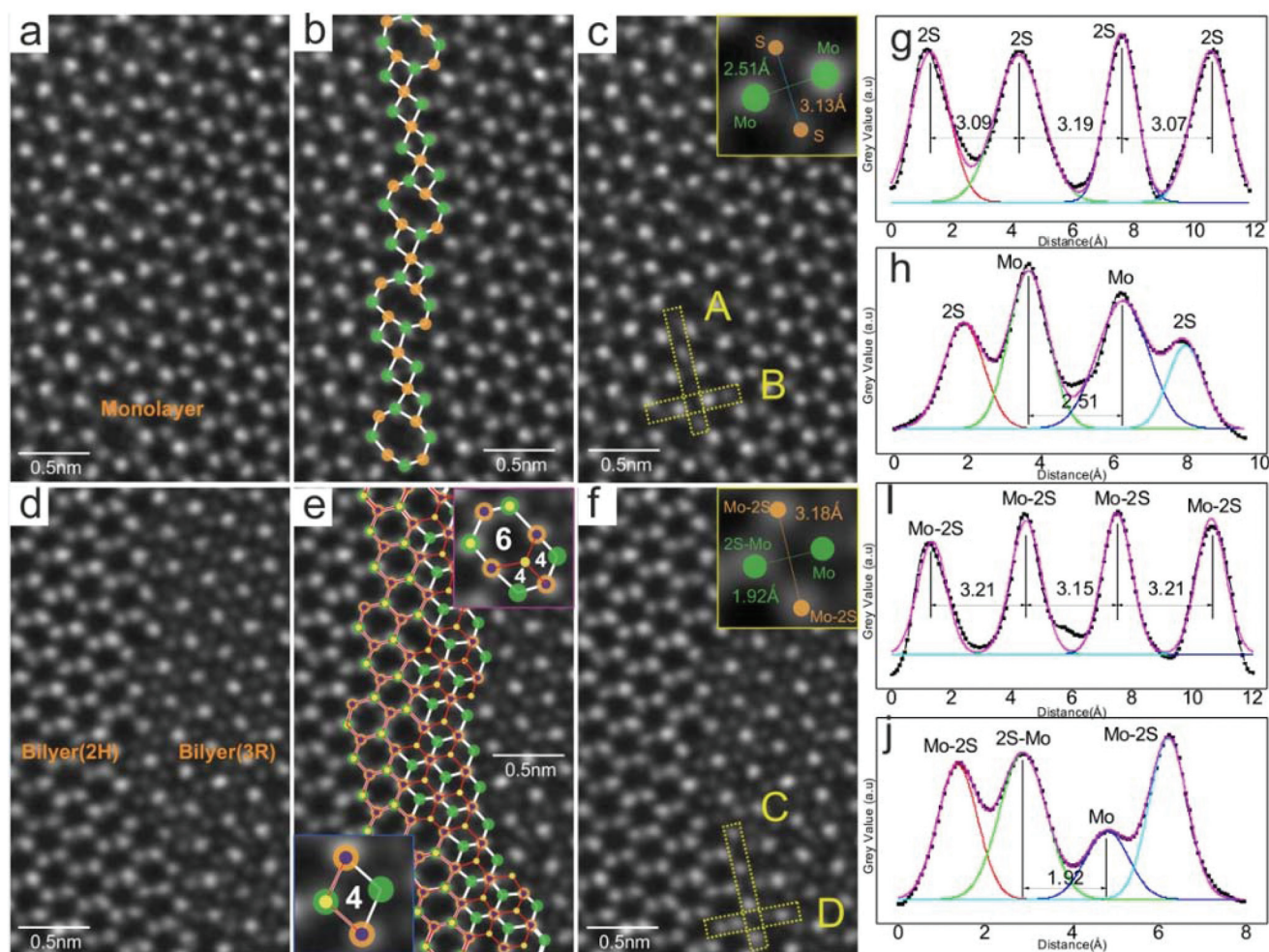


Fig. 3 (a) ADF-STEM image of an antiphase GB in monolayer MoS₂. (b) The same region with the atomic structure overlaid. (c) The region shown in (a) with an inset showing the column distances in a 4-member ring. (d) ADF-STEM image of an antiphase GB in bilayer MoS₂. (e) The same region with the atomic structure and insets showing the dislocation core structure. The inset shows the column distances in a 4-member ring. (f) The region shown in (e) with an inset showing the column distances in a 4-member ring. (g–j) Boxed line intensity profiles taken along the directions A–D, respectively. Regions indicated by yellow boxed areas in (c) and (f). All distances are normalized by the lattice parameters of pristine MoS₂ monolayers.

ing blocks of the antiphase boundary in monolayer. The same dislocation cores in bilayer region lead to sharp stacking transition from 2H to 3R in Fig. 2k. Schematic in Fig. 2l demonstrates that the 4-member ring embedded in the bottom layer of a bilayer system has more significant in-plane contraction, contributing to perfect stacking sequences.

Higher magnification ADF-STEM images of zone A and C with the antiphase boundaries are shown in Fig. 3a and d, respectively. In the monolayer region, the antiphase GB introduces a mirror symmetric domain rotated by 60° with respect to the original lattice and in which the Mo and S sites are swapped. The overlaid atomic structure in Fig. 3b indicates that the antiphase domains are joined by edge-sharing 4- and 8-member rings, similar to prior reports on MoS₂ GBs.³⁶ For the 4-member ring structure, Mo atoms retain 6-fold coordination whereas the S atoms change from 3-fold to 4-fold coordination changing the local stoichiometry from MoS₂ to Mo₄S₆ along the antiphase GB.³⁶ For the bilayer system, superimposed atomic structures shown in Fig. 3e reveal two distinct stacking sequences denoted as 2H and 3R when one layer is overlaid on the other layer including the antiphase GB. The 4-member ring retains its configuration, whereas the 8-membered core appears as 6–4–4 motif in projection due to the 3R stacking sequence on the right-hand side of the boundary. The 4-member rings in both monolayer and bilayer regions are compared in detail in Fig. 3c and f. The S–S and Mo–Mo

(monolayer) or (Mo–2S)–(Mo–2S) and (2S–Mo)–Mo (bilayer) column distances were using boxed intensity profiles along the zigzag (A and C) and armchair (B and D) directions. Average values were obtained through multiple measurements from different regions. Due to the lattice distortion along these two directions in our experimental images (Fig. S2†), the distance measurement was normalized using the pristine MoS₂ lattice parameter as a reference. Within the 4-member ring in the monolayer, the S column distances show similar values (3.13 Å vs. 3.18 Å), whereas a $\sim 24\%$ shrinkage in Mo column distances is observed in the bilayer.

To further study the reduction of the Mo–Mo distance in the 4-member rings, DFT calculations of both monolayer and bilayer MoS₂ systems were performed with a 4–4 chain along the zigzag direction as shown in Fig. 4. A multislice image simulation based on the DFT relaxed model of the bilayer system is shown in Fig. 4d and compared with our experimental image (Fig. 4c). Boxed intensity profiles were taken along direction 1 and 2 in both simulated and experimental images, and show excellent agreement. These results confirm that the antiphase boundary defects in the bottom layer lead to the atomically sharp transition between 2H and 3R stacking sequences. Fig. 4a and b compare the antiphase GB structure in the bottom layer of a bilayer and a monolayer, respectively. Insets in Fig. 4a and b show the bond lengths, indicating negligible difference in S–S column distances but a large discre-

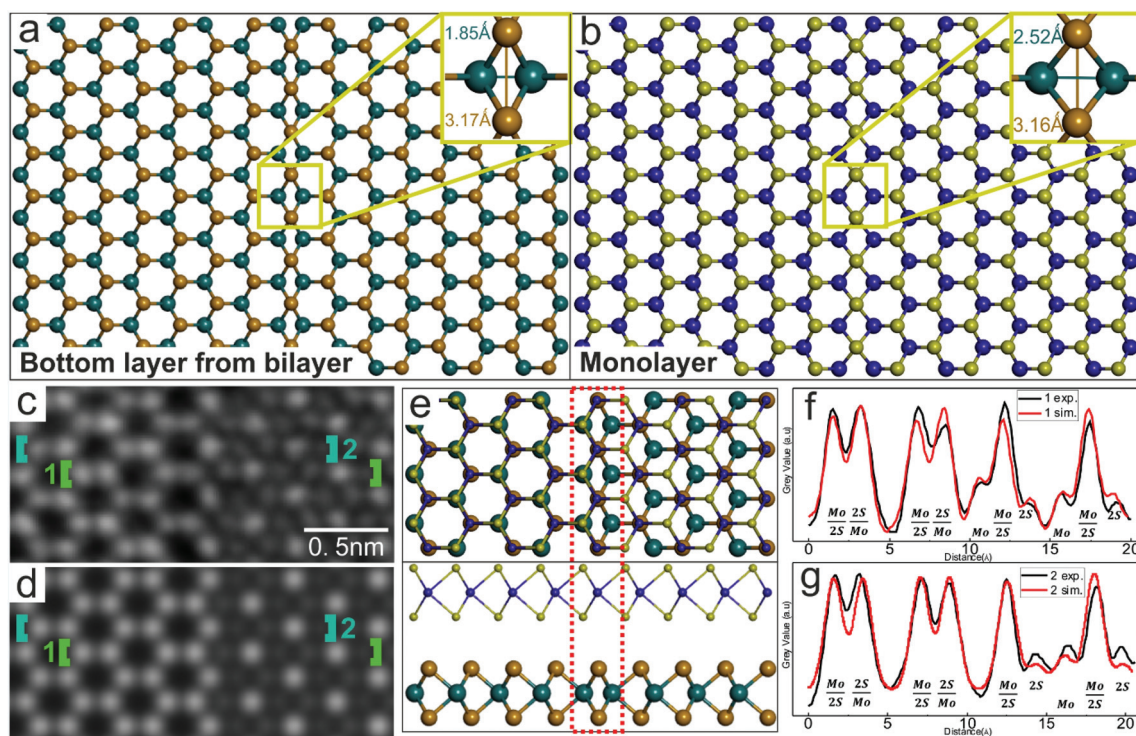


Fig. 4 DFT-relaxed models of a monolayer antiphase GB (a) extracted from a bilayer and (b) from a pure monolayer. The insets show the column distances in the 4-member rings. (c) ADF-STEM image of a bilayer region with an atomically sharp 2H–3R stacking interface from the antiphase GB in one layer. (d) Multislice image simulation based on the atomic arrangement calculated in (e) from the DFT-relaxed model. The position of 4-member defects is highlighted in red. (f and g) Boxed intensity line profiles taken from (c) experimental and (d) simulated images along the directions marked 1 and 2, respectively. Widths of boxes are indicated by the brackets in (c) and (d).

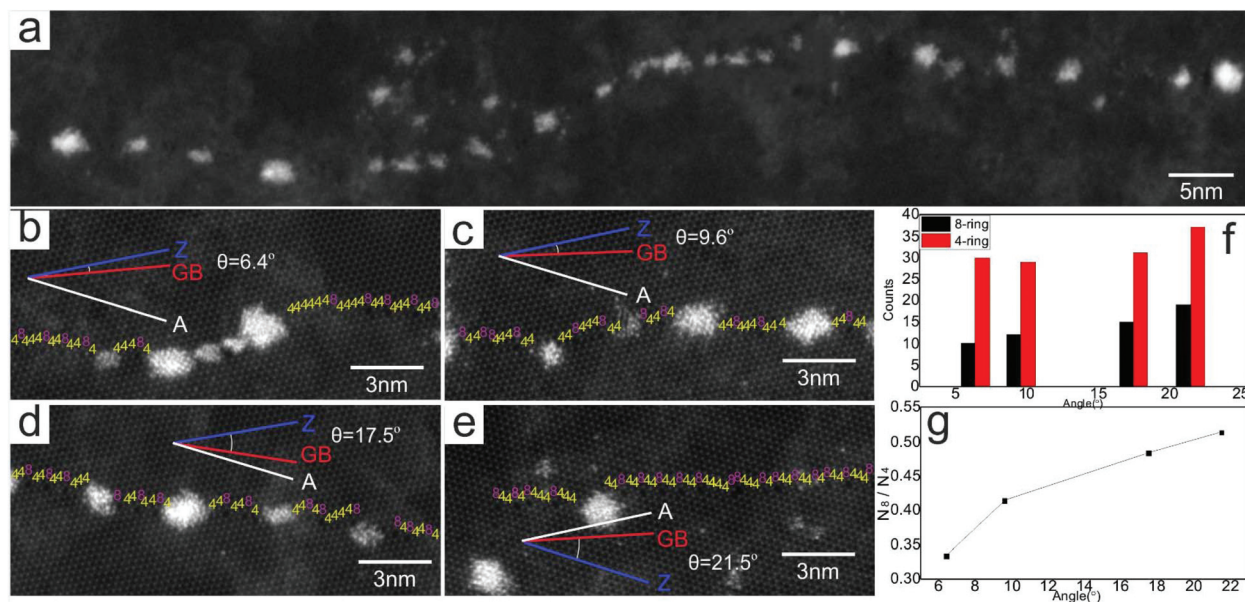


Fig. 5 (a) ADF-STEM image of an antiphase GB in monolayer MoS₂, tracked by the Pt cluster decoration. Segments deviate from zigzag directions by an angle, θ between (b) 6.4°, (c) 9.6°, (d) 17.5°, (e) 21.5°. Specific directions (Z for zigzag, GB for propagation and A for armchair) are indicated. (f) Histogram of 4- and 8-member rings varying with θ . (g) ratio of 8-ring/4-ring in b–e as a function of θ .

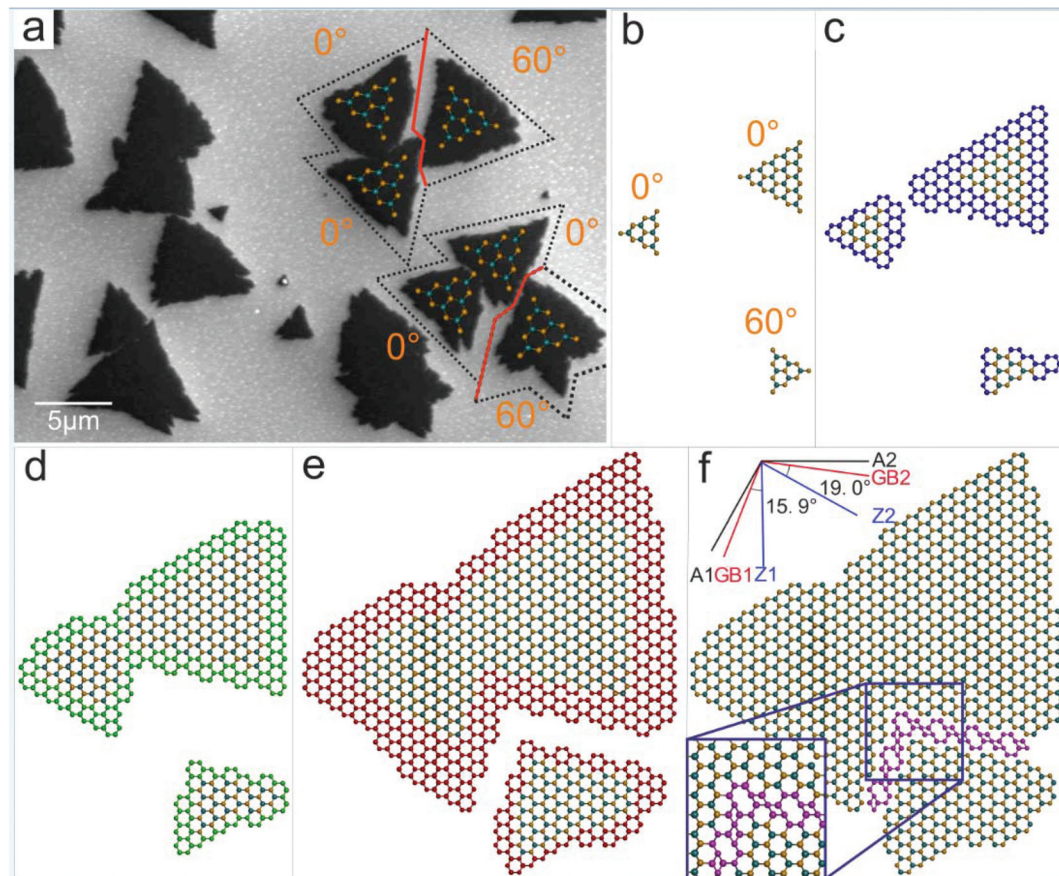


Fig. 6 (a) SEM image showing the irregular shape of MoS₂ domains grown on a Si/SiO₂ wafer by CVD. Grains are superimposed with atomic structures to indicate orientation differences. Angles shown are relative to the reference domain in each group. The meandering antiphase GBs formed by merging grains are highlighted by red. (b–f) Schematic atomic models illustrating the growth process of two antiphase GBs with a turning angle of $\sim 95^\circ$ which are connected by one 8-member ring at the apex.

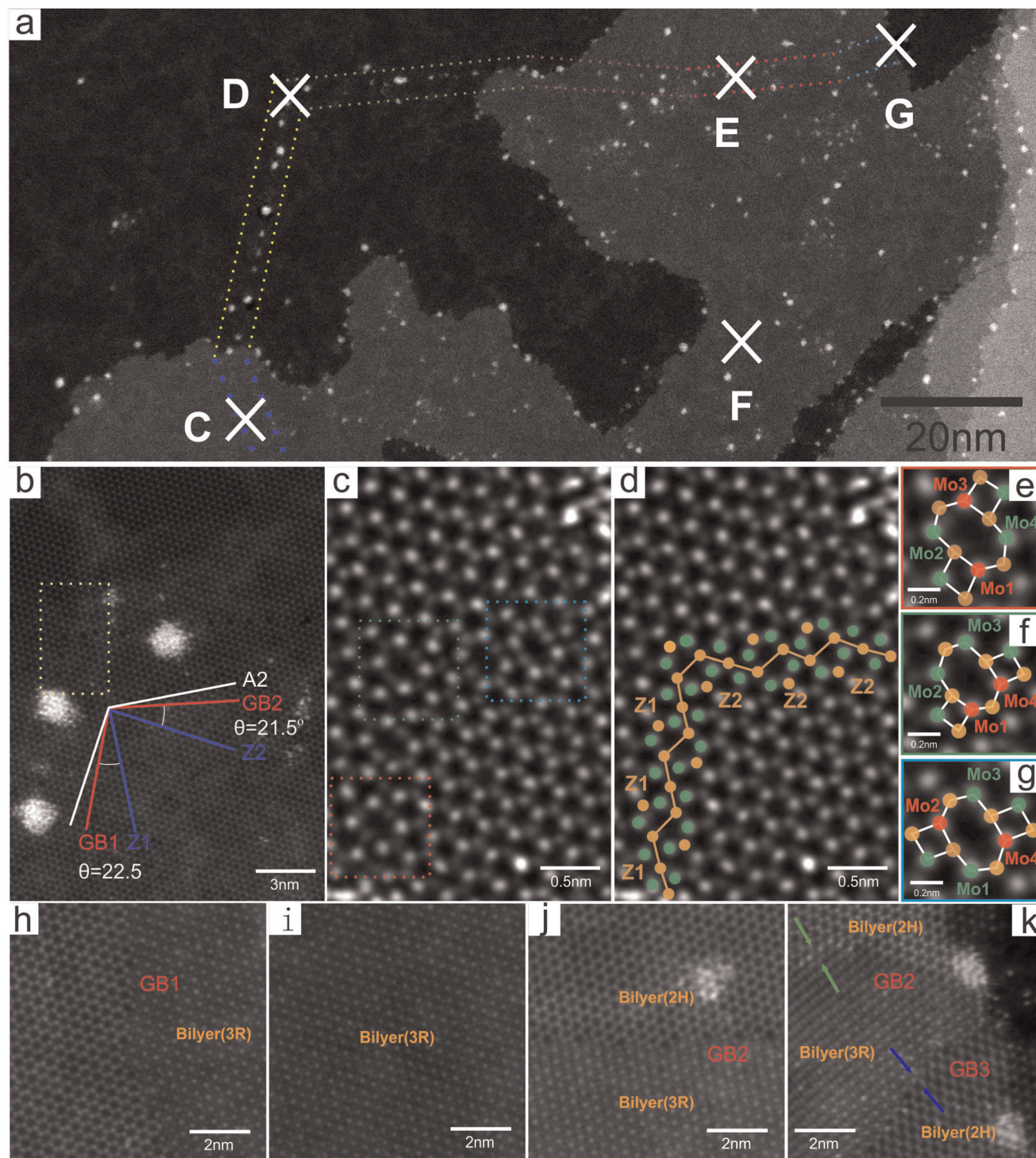


Fig. 7 (a) Low magnification image showing the top-side part in Fig. 2h. (b) ADF-STEM image showing large turning angle for an antiphase GB. Armchair (A1 and A2), zigzag (Z1 and Z2) and propagation directions (GB1 and GB2) are marked in white, blue and red, respectively. (c) ADF-STEM image showing the apex of the two antiphase GB directions. (d) Schematic illustration of the pathway of the antiphase GB superimposed on the ADF-STEM image in (b). (e–g) 8-Member defects that enable GB kinks, superimposed with atomic structures. Images are taken from the boxed areas in (e) the left-hand side (f) the center and (g) the right-hand side of the apex of two antiphase GBs. (h–j) ADF-STEM images showing how the large GB turning angle impacts the bilayer 2H and 3R stacking from zones C, F and E. (k) Region at the end of zone E, where the GB takes another large turn and causes local stacking changes of 2H and 3R. Contraction directions described in the text are indicated by green and blue arrows.

pancy in Mo–Mo column distances (2.25 Å for the monolayer and 1.85 Å for the bilayer corresponding to a shrinkage of ~22%), which is similar to our experimental observations. Similar phenomena have been reported in monolayer graphene, where a ridge structure was found to separate fcc and hcp domains of a graphene/Ni(111) interface.⁵² This bulging of graphene from the Ni(111) substrate facilitates matching of these two stacking sequences in a continuous film without any topological defects. In our case, this local in-plane compression perpendicular to the antiphase GB enables matching of the 2H and 3R stacking without any large out-of-plane distortion.

Fig. 5a shows a long section of the antiphase GB in a monolayer with different directions. The propagation direction of each segment is tilted from the zigzag direction by an angle θ , which ranges from 6.4° to 21.5° (as shown in Fig. 5b–e). The defects are highlighted in each segment and their numbers are shown in Fig. 5f. The 4-member rings outnumber the 8-member rings in all segments, and the ratio (N8/N4) is as low as 0.33 for Fig. 5b and as high as 0.51 in Fig. 5e. The ratio (N8/N4) as a function of θ (Fig. 5g) shows increased octagonal ring density with increasing θ . At the atomic level, 4-member rings provide GB propagation along the zigzag direction, whereas the 8-member rings provide arm-chair propagation, and the combination of these determines the arbitrary direction propagation. The ratio would equal 0 and 1 respectively if the GB propagated along the zigzag ($\theta = 0^\circ$) and the armchair direction ($\theta = 30^\circ$), respectively. Antiphase GBs act as 1D metallic wires embedded in the semiconducting MoS₂ matrix and kinks induce significant changes to the electronic behavior of a GB.³⁷ Alternatively, an antiphase GB has been reported to be n-doped due to the local Mo-rich environment arising from 4-member rings.^{36,37} The n-doped GB shows significant PL quenching due to an increased electron density,³⁶ suggesting that lower PL intensity quenching could be achieved with a higher 8-member ring density.

We now discuss a possible growth process that could lead to antiphase GBs between multiple grains. Fig. 6a shows an SEM image of MoS₂ grains with irregular shapes. The morphological irregularity is attributed to various factors including: growth temperature, presence of impurities, local Mo/S source concentration fluctuation and substrate effects. Two groups of grains, each of which contains three grains, are of particular interest. In each group, two grains sharing a common orientation exhibit a 60° rotation with respect to a third grain. Three grains can merge (as indicated in Fig. 6) and a meandering antiphase GB forms at a certain stage of growth. These observations are consistent with the GB formation mechanism described by Huang *et al.*⁵³ Initially, a group of grains with S-terminated zigzag edges nucleate on a bare substrate (Fig. 6b). The edges of each grain subsequently grow at uneven speeds and hence the grains show irregular morphologies (Fig. 6c). Two grains with the same orientation then merge (Fig. 6d) and continue to grow until they contact the 60° rotated grain (Fig. 6e). As shown in Fig. 6f, this mechanism gives rise to two segments of an antiphase GB with an angle of ~95° between the grains and a special 8-member ring at the apex that facilitates the large directional change of the antiphase GB.

Fig. 7a shows the top side part of Fig. 2h. Fig. 7b shows magnified zone D where a large directional change of the antiphase GB occurs, similar to that proposed in Fig. 6. At this location two antiphase GB segments (GB1 and GB2) meet with a rotation angle of ~104°. Both segments show a similar tilt angle (21.5° and 22.5°) from their respective zigzag directions, indicating a negligible difference in the 8-member ring density. The meeting point of the antiphase GB is examined at the atomic-level in Fig. 7c and d, qualitatively matching the structure in Fig. 7f. Fig. 7e–g compare the 8-member ring at the turning point to those in the other sections of the GB. Mo atoms in the alternative positions (Mo1 and Mo3 or Mo2 and Mo4) connect 4-member rings along the same zigzag directions, whereas neighboring Mo atoms (Mo1 and Mo4) at the meeting point facilitate directional switching from Z1 to Z2. Fig. 7h–j show how the change in angle of the antiphase GB influences the same bilayer domain by examining zones C, F and E. Zone C, which is associated with GB1 direction has the 2H:3R change (Fig. 7h), and the 3R stacking is maintained all the way to zone F (Fig. 7i), but at zone E (associated with GB2 direction), we see a reversal of the stacking from 3R:2H (Fig. 7j). However, Fig. 7k shows a region at the zone G, within the bilayer where the antiphase GB has another sharp turn and this induces local 2H–3R–2H changes. The 3R section in the middle, Fig. 7k, has blurred lattice contrast, indicating poor lattice registration within the 3R stacking, which is due to the competing strain effects of the GBs in different directions.

Conclusion

We have demonstrated that the propagation of an anti-phase GB from a MoS₂ monolayer into a bilayer region causes atomically sharp stacking changes from 2H–3R, which is reversed upon a second antiphase GB crossing. Antiphase GBs within the monolayer section can propagate with arbitrary direction by the combination of 4-fold and 8-fold rings, where the ratio depends upon GB angle relative to the zig-zag lattice direction of MoS₂. Large turning angles of the anti-phase GB were also observed and are mediated by a specific 8-member ring defect that has different positions of the attaching 4-member rings. Anti-phase GBs in the MoS₂ bilayer region exhibit larger lattice shrinkage along the Mo–Mo direction compared to the pure monolayers which is confirmed by DFT calculations. Overall, our data show that there is an energetic competition between a perfect 2H–3R stacking interface and in-plane bonding, in which interlayer van der Waals forces cause a bond contraction in MoS₂ due to antiphase GBs in order to achieve atomically sharp 2H–3R stacking sequences in the bilayer. These results provide a detailed characterization of antiphase GBs in monolayer MoS₂ and will help guide the understanding of their structure–property correlation. The observation of atomically sharp interface states may offer unique transport properties, given that topological confinement states can be created in 2D systems. Prior work has shown that graphene nanoroads in hBN sheets have 1D transport channels,⁵⁴ and that spatial vari-

ation of the interlayer potential difference in bilayer graphene also gives rise to topologically protected 1D states.^{55,56} Future work on the interfaces described in our manuscript here may also reveal such unique 1D confined states.

Methods

MoS₂ CVD synthesis and transfer

Synthesis of MoS₂ was carried out in two individually controlled quartz tube furnaces with Ar flowing at atmospheric pressure over S (1 g of purum grade >99.5%) and MoO₃ powders. The MoO₃ precursor was initially loaded in a 1 cm diameter tube, which was in turn placed inside the larger diameter 1 in tube of the CVD furnace. This prevented cross-contamination of S and MoO₃ prior to MoS₂ formation on the target substrate, with the S separated in the larger diameter outer tube. Two furnaces were used to control the temperature of each precursor and the substrate, with heating temperatures for S = 180 °C, MoO₃ = 300 °C, with the substrate held at 800 °C. Ar was used as a carrier gas. The S initially vaporized for 15 min, before the temperature of the second furnace was increased to 800 °C at 40 °C min⁻¹ and left for 15 min under an Ar flow of 150 sccm. The Ar flow was then reduced to 10 sccm for 25 min, followed by a fast cooling (sample removal). The S temperature was kept at 180 °C throughout.

The as-grown sample was spin coated with a PMMA scaffold (8 wt% in anisole, 495k molecular weight) at 4700 rpm for 60 s and then cured at 150 °C for 15 min. The edge of the wafer was then ground with a diamond file to expose the SiO₂/Si edges to an etchant solution. The underlying SiO₂/Si substrate was detached by floating the sample on a 15 M KOH (Sigma-Aldrich) solution in a water bath for 2 h at 40 °C. The resultant suspended PMMA-MoS₂ film was thoroughly cleaned by several transfers to DI water. For the STEM characterization, the PMMA-MoS₂ film was transferred onto a holey Si₃N₄ grid and dried overnight in air. The PMMA-MoS₂-Si₃N₄ was finally baked at 150 °C for 15 min to improve sample adhesion and the PMMA was subsequently removed using acetone for 24 h.

Scanning transmission electron microscopy

Room temperature ADF-STEM was performed using an aberration corrected JEOL ARM300CF STEM equipped with a JEOL ETA corrector⁵⁷ operated at an accelerating voltage of 60 kV located in the electron Physical Sciences Imaging Centre (ePSIC) at Diamond Light Source. The convergence semi-angle used was 24.6 mrad with a camera length of 20 cm, corresponding to an annular recording range of 39–156 mrad at the detector plane. The electron probe diameter was focused to ~72 pm with a dwell time ranging from 10–20 μs per pixel for imaging. The beam current was measured as 23 pA.

Image simulations and processing

Multislice ADF image simulations used the JEMS software package. ImageJ was used to process the ADF-STEM images. A bandpass filter (between 100 and 1 pixels) and a Gaussian blur

(2 pixels) were applied to minimize the long-range effects in intensity due to uneven illumination.

Density functional theory (DFT) calculation

The DFT simulations were conducted using the Vienna *Ab initio* Simulation Package.⁵⁸ The Perdew–Burke–Ernzerhof exchange-correlational functional,⁵⁹ and the projector augmented wave method were employed in our calculations.⁶⁰ DFT calculations of both monolayer and bilayer MoS₂ systems (consisting of 180 and 360 atoms, respectively) were performed. A vacuum layer of 10 Å was included to reflect the 2D nature of the material. A plane wave basis set with an energy cutoff of 300 eV was adopted to expand the electronic wave functions. The Brillouin zone integration was conducted on a 1 × 27 × 2 Monkhorst–Pack *k*-point mesh,⁶¹ and the atomic coordinates in all structures were relaxed until the maximum residual force was below 0.02 eV Å⁻¹.

Conflicts of interest

There are no conflicts to declare.

Acknowledgements

J. H. W. thanks the support from the Royal Society and the European Research Council (Grant No: 725258 CoG 2016 LATO). A. I. K. acknowledges financial support from EPSRC (Platform Grants EP/F048009/1 and EP/K032518/1) and from the EU (ESTEEM2 (Enabling Science and Technology through European Electron Microscopy)), 7th Framework Programme of the European Commission. J. L. acknowledges support by NSF DMR-1410636.

References

- 1 Y. Gong, J. Lin, X. Wang, G. Shi, S. Lei, Z. Lin, X. Zou, G. Ye, R. Vajtai, B. I. Yakobson, *et al.*, Vertical and In-plane Heterostructures from WS₂/MoS₂ Monolayers, *Nat. Mater.*, 2014, **13**, 1135–1142.
- 2 G. Plechinger, P. Nagler, J. Kraus, N. Paradiso, C. Strunk, C. Schüller and T. Korn, Identification of Excitons, Trions and Biexcitons in Single-layer WS₂, *Phys. Status Solidi RRL*, 2015, **9**, 457–461.
- 3 F. Withers, T. H. Bointon, D. C. Hudson, M. F. Craciun and S. Russo, Electron Transport of WS₂ Transistors in a Hexagonal Boron Nitride Dielectric Environment, *Sci. Rep.*, 2014, **4**, 4967.
- 4 V. Sorkin, H. Pan, H. Shi, S. Y. Quek and Y. W. Zhang, Nanoscale Transition Metal Dichalcogenides: Structures, Properties, and Applications, *Crit. Rev. Solid State Mater. Sci.*, 2014, **39**, 319–367.
- 5 H.-P. Komsa, J. Kotakoski, S. Kurasch, O. Lehtinen, U. Kaiser and A. V. Krasheninnikov, Two-Dimensional Transition Metal Dichalcogenides under Electron

- Irradiation: Defect Production and Doping, *Phys. Rev. Lett.*, 2012, **109**, 1–5.
- 6 Q. H. Wang, K. Kalantar-Zadeh, A. Kis, J. N. Coleman and M. S. Strano, Electronics and Optoelectronics of Two-Dimensional Transition Metal Dichalcogenides, *Nat. Nanotechnol.*, 2012, **7**, 699–712.
 - 7 Y. Ma, Y. Dai, M. Guo, C. Niu, J. Lu and B. Huang, Electronic and Magnetic Properties of Perfect, Vacancy-Doped, and Nonmetal Adsorbed MoSe₂, MoTe₂ and WS₂ Monolayers, *Phys. Chem. Chem. Phys.*, 2011, **13**, 15546–15553.
 - 8 Y. H. Lee, X. Q. Zhang, W. Zhang, M. T. Chang, C. T. Lin, K. D. Chang, Y. C. Yu, J. T. W. Wang, C. S. Chang, L. J. Li and T. W. Lin, Synthesis of Large-area MoS₂ Atomic Layers with Chemical Vapor Deposition, *Adv. Mater.*, 2012, **24**(17), 2320–2325.
 - 9 Y. Zhan, Z. Liu, S. Najmaei, P. M. Ajayan and J. Lou, Large-area Vapor-phase Growth and Characterization of MoS₂ Atomic Layers on a SiO₂ Substrate, *Small*, 2012, **8**(7), 966–971.
 - 10 K. K. Liu, W. Zhang, Y. H. Lee, Y. C. Lin, M. T. Chang, C. Y. Su, C. S. Chang, H. Li, Y. Shi, H. Zhang and C. S. Lai, Growth of Large-area and Highly Crystalline MoS₂ Thin Layers on Insulating Substrates, *Nano Lett.*, 2012, **12**(3), 1538–1544.
 - 11 Y. Shi, W. Zhou, A. Y. Lu, W. Fang, Y. H. Lee, A. L. Hsu, S. M. Kim, K. K. Kim, H. Y. Yang, L. J. Li and J. C. van der Waals, Epitaxy of MoS₂ Layers Using Graphene as Growth Templates, *Nano Lett.*, 2012, **12**(6), 2784–2791.
 - 12 B. Radisavljevic, A. Radenovic, J. Brivio, I. V. Giacometti and A. Kis, Single-layer MoS₂ Transistors, *Nat. Nanotechnol.*, 2011, **6**(3), 147–150.
 - 13 C. R. Dean, A. F. Young, I. Meric, C. Lee, L. Wang, S. Sorgenfrei, K. Watanabe, T. Taniguchi, P. Kim, K. L. Shepard and J. Hone, Boron Nitride Substrates for high-quality Graphene Electronics, *Nat. Nanotechnol.*, 2010, **5**(10), 722–726.
 - 14 L. Britnell, R. V. Gorbachev, R. Jalil, B. D. Belle, F. Schedin, A. Mishchenko, T. Georgiou, M. I. Katsnelson, L. Eaves, S. V. Morozov and N. M. R. Peres, Field-effect Tunneling Transistor based on Vertical Graphene Heterostructures, *Science*, 2012, **335**(6071), 947–950.
 - 15 K. F. Mak, C. Lee, J. Hone, J. Shan and T. F. Heinz, Atomically Thin MoS₂: A New Direct-gap Semiconductor, *Phys. Rev. Lett.*, 2010, **105**(13), 136805.
 - 16 Z. Yin, H. Li, H. Li, L. Jiang, Y. Shi, Y. Sun, G. Lu, Q. Zhang, X. Chen and H. Zhang, Single-Layer MoS₂ Phototransistors, *ACS Nano*, 2011, **6**(1), 74–80.
 - 17 Q. Yu, L. A. Jauregui, W. Wu, R. Colby, J. Tian, Z. Su, H. Cao, Z. Liu, D. Pandey, D. Wei and T. F. Chung, Control and Characterization of Individual Grains and Grain Boundaries in Graphene Grown by Chemical Vapor Deposition, *Nat. Mater.*, 2011, **10**(6), 443–449.
 - 18 J. D. Wood, S. W. Schmucker, A. S. Lyons, E. Pop and J. W. Lyding, Effects of Polycrystalline Cu Substrate on Graphene Growth by Chemical Vapor Deposition, *Nano Lett.*, 2011, **11**(11), 4547–4554.
 - 19 L. P. Biró and P. Lambin, Grain Boundaries in Graphene Grown by Chemical Vapor Deposition, *New J. Phys.*, 2013, **15**(3), 035024.
 - 20 H. Hilgenkamp and J. Mannhart, Grain Boundaries in High-T Superconductors, *Rev. Mod. Phys.*, 2002, **74**(2), 485.
 - 21 C. S. Pande and K. P. Cooper, Nanomechanics of Hall-Petch Relationship in Nanocrystalline Materials, *Prog. Mater. Sci.*, 2009, **54**(6), 689–706.
 - 22 I. Ovidko, Review on Grain Boundaries in Graphene. Curved Poly- and nanocrystalline Graphene Structures as New Carbon Allotropes, *Rev. Adv. Mater. Sci.*, 2012, **30**(3), 201–224.
 - 23 L. Zhao, K. T. Rim, H. Zhou, R. He, T. F. Heinz, A. Pinczuk, G. W. Flynn and A. N. Pasupathy, Influence of Copper Crystal Surface on the CVD Growth of Large Area Monolayer Graphene, *Solid State Commun.*, 2011, **151**(7), 509–513.
 - 24 S. Malola, H. Häkkinen and P. Koskinen, Structural, Chemical, and Dynamical Trends in Graphene Grain Boundaries, *Phys. Rev. B: Condens. Matter Mater. Phys.*, 2010, **81**(16), 165447.
 - 25 E. Cockayne, G. M. Rutter, N. P. Guisinger, J. N. Crain, P. N. First and J. A. Stroscio, Grain Boundary Loops in Graphene, *Phys. Rev. B: Condens. Matter Mater. Phys.*, 2011, **83**(19), 195425.
 - 26 K. S. Kim, Y. Zhao, H. Jang, S. Y. Lee, J. M. Kim, K. S. Kim, J. H. Ahn, P. Kim, J. Y. Choi and B. H. Hong, Large-Scale Pattern Growth of Graphene Films for Stretchable Transparent Electrodes, *Nature*, 2009, **457**, 706–710.
 - 27 A. Reina, X. Jia, J. Ho, D. Nezich, H. Son, V. Bulovic, M. S. Dresselhaus and J. Kong, Large Area, Few-Layer Graphene Films on Arbitrary Substrates by Chemical Vapor Deposition, *Nano Lett.*, 2009, **9**, 30–35.
 - 28 X. Li, W. Cai, J. An, S. Kim, J. Nah, D. Yang, R. Piner, A. Velamakanni, I. Jung, E. Tutuc, *et al.*, Large-Area Synthesis of High-Quality and Uniform Graphene Films on Copper Foils, *Science*, 2009, **324**, 1312–1314.
 - 29 S. Bae, H. K. Kim, Y. Lee, X. Xu, J. S. Park, Y. Zheng, J. Balakrishnan, T. Lei, H. R. Kim, Y. I. Song, *et al.*, Roll-to-Roll Production of 30-Inch Graphene Films for Transparent Electrodes, *Nat. Nanotechnol.*, 2010, **5**, 574–578.
 - 30 W. Cai, A. L. Moore, Y. Zhu, X. Li, S. Chen, L. Shi and R. S. Ruoff, Thermal Transport in Suspended and Supported Monolayer Graphene Grown by Chemical Vapor Deposition, *Nano Lett.*, 2010, **10**, 1645–1651.
 - 31 R. Grantab, V. B. Shenoy and R. S. Ruoff, Anomalous Strength Characteristics of Tilt Grain Boundaries in Graphene, *Science*, 2010, **330**, 946–948.
 - 32 O. V. Yazyev and S. G. Louie, Electronic Transport in Polycrystalline Graphene, *Nat. Mater.*, 2010, **9**, 806–809.
 - 33 K. S. Novoselov, D. Jiang, F. Schedin, T. J. Booth, V. V. Khotkevich, S. V. Morozov and A. K. Geim, Two-Dimensional Atomic Crystals, *Proc. Natl. Acad. Sci. U. S. A.*, 2005, **102**, 10451–10453.
 - 34 A. N. Enyashin, M. Bar-Sadan, L. Houben and G. Seifert, Line Defects in Molybdenum Disulfide Layers, *J. Phys. Chem. C*, 2013, **117**, 10842–10848.

- 35 H. Qiu, T. Xu, Z. Wang, W. Ren, H. Nan, Z. Ni, Q. Chen, S. Yuan, F. Miao, F. Song, *et al.*, Hopping Transport Through Defect-Induced Localized States in Molybdenum Disulphide, *Nat. Commun.*, 2013, **4**, 2442.
- 36 A. M. Van Der Zande, P. Y. Huang, D. A. Chenet, T. C. Berkelbach, Y. You, G. H. Lee, T. F. Heinz, D. R. Reichman, D. A. Muller and J. C. Hone, Grains and Grain boundaries in Highly Crystalline Monolayer Molybdenum Disulphide, *Nat. Mater.*, 2013, **12**(6), 554–561.
- 37 W. Zhou, X. Zou, S. Najmaei, Z. Liu, Y. Shi, J. Kong, J. Lou, P. M. Ajayan, B. I. Yakobson and J. C. Idrobo, Intrinsic Structural Defects in Monolayer Molybdenum Disulfide, *Nano Lett.*, 2013, **13**(6), 2615–2622.
- 38 X. Zou, Y. Liu and B. I. Yakobson, Predicting Dislocations and Grain Boundaries in Two-Dimensional Metal-Disulfides from the First Principles, *Nano Lett.*, 2012, **13**(1), 253–258.
- 39 J. Lin, S. T. Pantelides and W. Zhou, Vacancy-Induced Formation and Growth of Inversion Domains in Transition-Metal Dichalcogenide Monolayer, *ACS Nano*, 2015, **9**(5), 5189–5197.
- 40 A. Azizi, X. Zou, P. Ercius, Z. Zhang, A. L. Elías, N. Perea-López, G. Stone, M. Terrones, B. I. Yakobson and N. Alem, Dislocation Motion and Grain Boundary Migration in Two-Dimensional Tungsten Disulphide, *Nat. Commun.*, 2014, **5**, 4867.
- 41 T. H. Ly, D. J. Perello, J. Zhao, Q. Deng, H. Kim, G. H. Han, S. H. Chae, H. Y. Jeong and Y. H. Lee, Misorientation-Angle-Dependent, *Nat. Commun.*, 2016, **7**, 10426.
- 42 X. Liu, I. Balla, H. Bergeron and M. C. Hersam, Point Defects and Grain Boundaries in Rotationally Commensurate MoS₂ on Epitaxial Graphene, *J. Phys. Chem. C*, 2016, **120**(37), 20798–20805.
- 43 S. Najmaei, Z. Liu, W. Zhou, X. Zou, G. Shi, S. Lei, B. I. Yakobson, J.-C. Idrobo, P. M. Ajayan and J. Lou, Vapour Phase Growth and Grain Boundary Structure of Molybdenum Disulphide Atomic Layers, *Nat. Mater.*, 2013, **12**, 754–759.
- 44 S. Najmaei, M. Amani, M. L. Chin, Z. Liu, A. G. Birdwell, T. P. O'Regan, P. M. Ajayan, M. Dubey and J. Lou, Electrical Transport Properties of Polycrystalline Monolayer Molybdenum Disulfide, *ACS Nano*, 2014, **8**, 7930–7937.
- 45 W. Guo, B. Wu, Y. Li, L. Wang, J. Chen, B. Chen, Z. Zhang, L. Peng, S. Wang and Y. Liu, Governing Rule for Dynamic Formation of Grain Boundaries in Grown Graphene, *ACS Nano*, 2015, **9**(6), 5792–5798.
- 46 K. Elibol, T. Susi, O. Maria, B. C. Bayer, T. J. Pennycook, N. McEvoy, G. S. Duesberg, J. C. Meyer and J. Kotakoski, Grain Boundary-Mediated Nanopores in Molybdenum Disulfide Grown by Chemical Vapor Deposition, *Nanoscale*, 2017, **9**, 1591–1598.
- 47 B. C. Bayer, S. Caneva, T. J. Pennycook, J. Kotakoski, C. Mangler, S. Hofmann and J. C. Meyer, Introducing Overlapping Grain Boundaries in Chemical Vapour Deposited Hexagonal Boron Nitride Monolayer Films, *ACS Nano*, 2017, **11**, 4521–4527.
- 48 X. Zhao, Z. Ding, J. Chen, J. Dan, S. M. Poh, W. Fu, S. J. Pennycook, W. Zhou and K. P. Loh, Strain Modulation by van der Waals Coupling in Bilayer Transition Metal Dichalcogenide, *ACS Nano*, 2018, **12**, 1940–1948.
- 49 S. Zhou, S. Wang, H. Li, W. Xu, C. Gong, J. C. Grossman and J. H. Warner, Atomic Structure and Dynamics of Defects in 2D MoS₂ Bilayers, *ACS Omega*, 2017, **2**(7), 3315–3324.
- 50 W. Rong, K. He, M. Pacios, A. W. Robertson, H. Bhaskaran and J. H. Warner, Controlled Preferential Oxidation of Grain Boundaries in Monolayer Tungsten Disulfide for Direction Optical Imaging, *ACS Nano*, 2015, **9**, 3695–3703.
- 51 S. Wang, H. Sawada, X. Han, S. Zhou, S. Li, Z. X. Guo, A. I. Kirkland and J. H. Warner, Preferential Pt Nanocluster Seeding at Grain Boundary Dislocations in Polycrystalline Monolayer MoS₂, *ACS Nano*, 2018, **12**, 5626–5636.
- 52 J. Lahiri, Y. Lin, P. Bozkurt, I. I. Oleynik and M. Batzill, An Extended Defect in Graphene as a Metallic Wire, *Nat. Nanotechnol.*, 2010, **5**, 326–329.
- 53 P. Y. Huang, C. S. Ruiz-Vargas, A. M. van der Zande, W. S. Whitney, M. P. Levendorf, J. W. Kevek, S. Garg, J. S. Alden, C. J. Hustedt, Y. Zhu and J. Park, Grains and Grain Boundaries in Single-Layer Graphene Atomic Patchwork Quilts, *Nature*, 2011, **469**(7330), 389–392.
- 54 J. Jung, Z. Qiao, Q. Niu and A. H. MacDonald, Transport Properties of Graphene Nanoroads in Boron Nitride Sheets, *Nano Lett.*, 2012, **12**, 2936–2940.
- 55 Z. Qiao, J. Jung, Q. Niu and A. H. MacDonald, Electronic Highways in Bilayer Graphene, *Nano Lett.*, 2011, **11**, 3453–3459.
- 56 I. Martin, Y. M. Blanter and A. F. Morpurgo, Topological Confinement in Bilayer Graphene, *Phys. Rev. Lett.*, 2008, **100**, 036804.
- 57 F. Hosokawa, H. Sawada, Y. Kondo, K. Takayanagi and K. Suenaga, Development of Cs and Cc Correctors for Transmission Electron Microscopy, *Microscopy*, 2013, **62**, 23–41.
- 58 G. Kresse and J. Furthmüller, Efficient Iterative Schemes for ab initio Total-Energy Calculations Using a Plane-Wave Basis set, *Phys. Rev. B: Condens. Matter Mater. Phys.*, 1996, **54**, 11169–11186.
- 59 J. P. Perdew, K. Burke and M. Ernzerhof, Generalized Gradient Approximation Made Simple, *Phys. Rev. Lett.*, 1996, **77**, 3865–3868.
- 60 P. E. Blöchl, Projector Augmented-wave Method, *Phys. Rev. B: Condens. Matter Mater. Phys.*, 1994, **50**, 17953–17979.
- 61 H. J. Monkhorst and J. D. Pack, Special Points for Brillouin-Zone Integrations, *Phys. Rev. B: Condens. Matter Mater. Phys.*, 1976, **13**, 5188–5192.

Atomically Sharp Interlayer Stacking Shifts at Anti-phase Grain Boundaries in Overlapping MoS₂

Secondary layers

Si Zhou¹, Shanshan Wang^{1,2}, Zhe Shi³, Hidetaka Sawada⁴, Angus I. Kirkland^{1,5}, Ju Li^{3,6}, Jamie H.

Warner^{1}*

¹Department of Materials, University of Oxford, 16 Parks Road, Oxford, OX1 3PH, United Kingdom

²Science and Technology on Advanced Ceramic Fibers & Composites Laboratory, National University of Defense Technology, Changsha 410073, Hunan Province, China

³Department of Materials Science and Engineering, MIT, 77 Massachusetts Ave, Cambridge, MA 02139, USA

⁴JEOL Ltd., 3-1-2 Musashino, Akishima, Tokyo 196-8558, Japan

⁵Electron Physical Sciences Imaging Center, Diamond Light Source Ltd, Didcot, UK

⁶Department of Nuclear Science and Engineering, MIT, 77 Massachusetts Ave, Cambridge, MA 02139, USA

Email: *Jamie.warner@materials.ox.ac.uk

Supporting Information

S1. ADF-STEM images of monolayer- bilayer interfaces

A bilayer region with an antiphase boundary is shown in Figure S1a. Two distinct stacking sequences with the boundary as interface can be identified by their unique contrast. The colored boxed regions showing the step edges are magnified in Figure S1b and c, respectively. Boxed line profile are taken along different directions for each step edge. Based on our previous experimental images and

Multislice simulation results, the atomic arrangements are displayed in Figure S1d and e to confirm that bilayer regions in Figure S1b and c are 2H and 3R stacked, respectively.

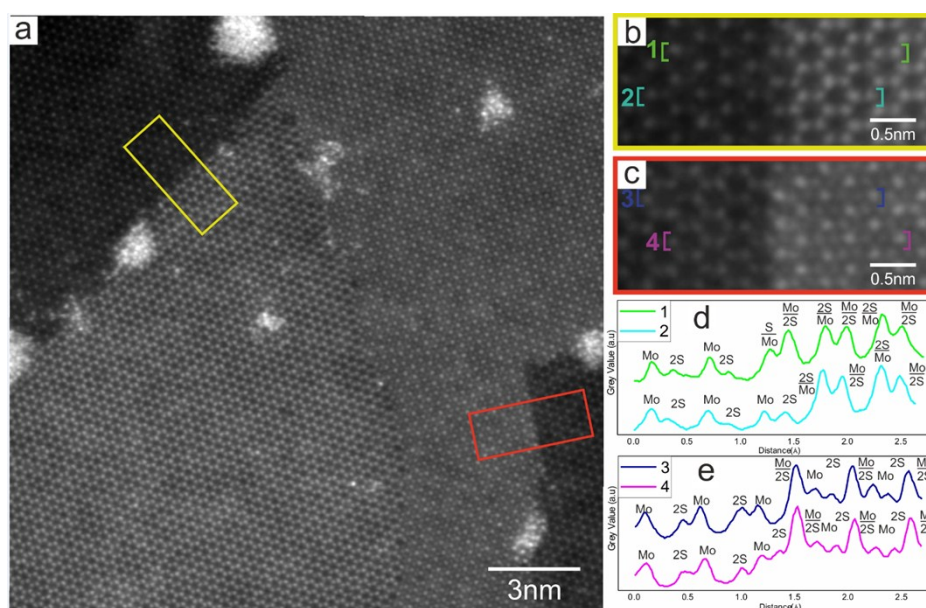


Figure S1. (a) ADF-STEM image showing the antiphase boundary propagating through a bilayer region. Two types of mono-bilayer interfaces are observed. (b and c) zoomed in images of the boxed regions in a. (d and e) Boxed line intensity profile along directions in b and c, respectively.

S2. Measurement of lattice distortion along zigzag and armchair directions

Figure S2a shows the same image we use for 4-fold ring column distance measurements in Figure 3. To take the lattice distortion, which happens due to local strain or coma and 2-fold astigmatism introduced in the image, into consideration, we conduct boxed line intensity profiles along the zigzag (direction 1) and armchair (direction 2) directions and display the results in Figure S2b and c, respectively. The average Mo-Mo distance along direction 1 is calculated as 0.313nm, exhibiting 0.95% shrinkage compared with the value in pristine MoS₂ (0.316nm). Similarly, the Mo-Mo distance along direction 2 is 0.555nm which is 1.4% higher than the standard value (0.547nm). Therefore, all measurements conducted in Figure 3 are normalized using the standard values as references.

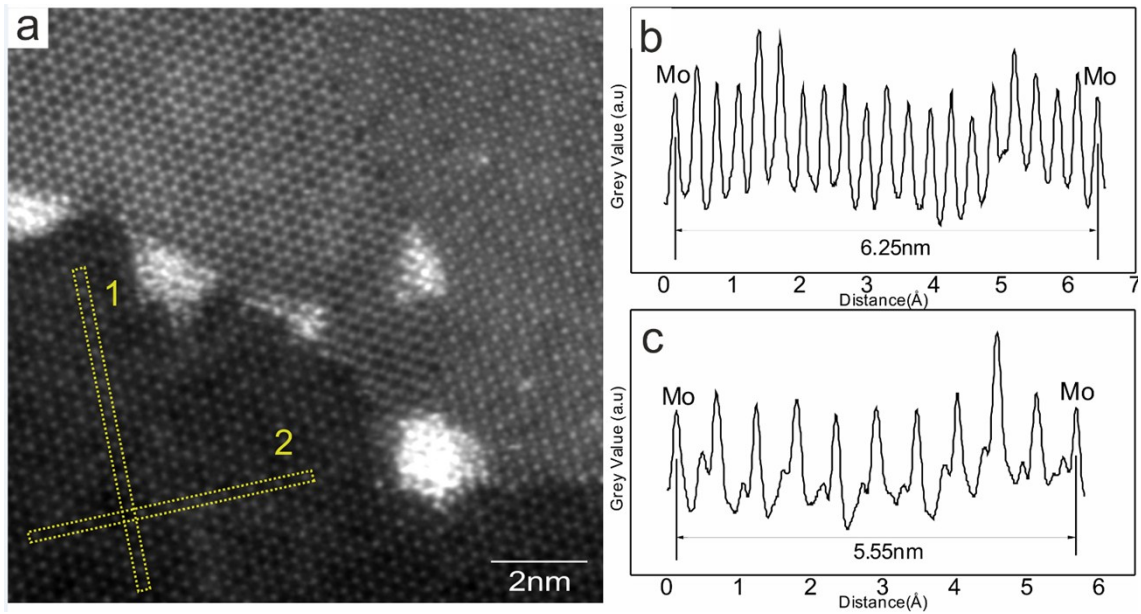


Figure S2. (a) The ADF-STEM image used for column distance measurement in Figure 3. (b and c) Boxed line intensity profile along direction 1 and 2, respectively.

S3. Dynamics of dislocation cores of the antiphase boundary in MoS₂ monolayers

Image frames in Figure S3 show local motif change during 6s under electron beam irradiation. The overlaid atomic structures in Figure S3a and d reveal that the structure only happens in the local 6-, 4- and 8- rings without affecting the propagation direction of the antiphase grain boundary. The 6-4-8 motif simply swaps to 8-4-6 motif. Based on the atomic models in Figure S3e-f, the reconstruction happens when one Mo atom is knocked out from position 1 and refills in position 2. It could also happen when Mo at position 1 migrates to position 2 along the armchair direction.

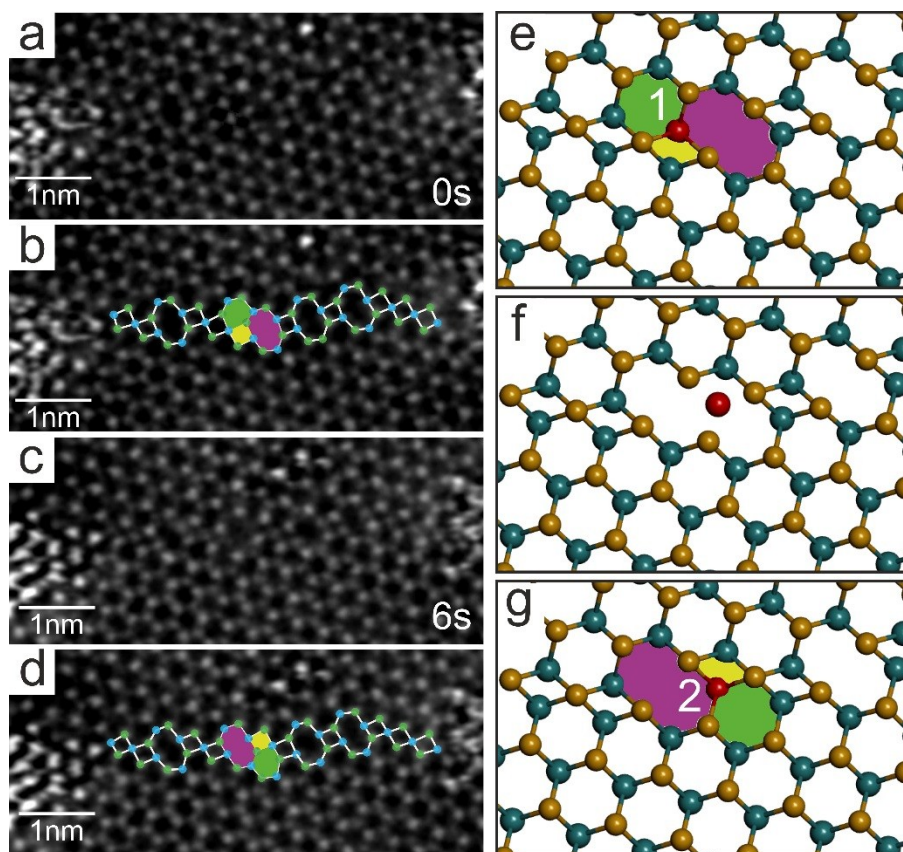


Figure S3. ADF-STEM images showing the same GB area at (a) 0s and (c) 6s. (b and d) image a and c with overlaid atomic structures, respectively, showing different local motif. (e-g) Atomic model of a single Mo atom escaping from position 1 and reappears in position 2.